Journal of Energy Chemistry 67 (2022) 814–823

Contents lists available at ScienceDirect

Journal of Energy Chemistry

journal homepage: www.elsevier.com/locate/jechem

http://www.journals.elsevier.com/journal-of-energy-chemistry/

High-performance solid-solution potassium-ion intercalation mechanism of multilayered turbostratic graphene nanosheets

Jiae Um [a], Seung Uk Yoon [b], Hoseong Kim [a], Beom Sik Youn [c], Hyoung-Joon Jin [a,b,*], Hyung-Kyu Lim [c,*], Young Soo Yun [d,e,*]

[a] Program in Environmental and Polymer Engineering, Inha University, Incheon 22212, South Korea
[b] Department of Polymer Science and Engineering, Inha University, Incheon 22212, South Korea
[c] Division of Chemical Engineering and Bioengineering, Kangwon National University, Chuncheon, Gangwon-do 24341, South Korea
[d] KU-KIST Graduate School of Converging Science and Technology, Korea University, 145 Anam-ro, Seongbuk-gu, Seoul 02841, South Korea
[e] Department of Integrative Energy Engineering, 145 Anam-ro, Seongbuk-gu, Korea University, Seoul 02841, South Korea

ARTICLE INFO

Article history:
Received 25 August 2021
Revised 10 November 2021
Accepted 13 November 2021
Available online 26 November 2021

Keywords:
Turbostratic graphite
Graphene nanosheet
Defective carbon
Anode
Potassium-ion batteries

ABSTRACT

The solid-solution reaction between an alkali cation and an active host material is known as a single-phase redox mechanism, and it is typically accompanied by a continuous voltage change. It is distinct from the typical alkali cation intercalation reaction at an equivalent site of the active host material, which exhibits a voltage plateau. Herein, we report an unusual solid-solution potassium-ion intercalation mechanism with a low-voltage plateau capacity on multilayered turbostratic graphene nanosheets (T-GNSs). Despite the disordered graphitic structure with a broad range of *d*-spacings (3.65–4.18 Å), the T-GNSs showed a reversible plateau capacity of ~ 200 mA h g^{-1}, which is higher than that of a well-ordered graphite nanoplate (~120 mA h g^{-1}). In addition, a sloping capacity of ~ 220 mA h g^{-1} was delivered with the plateau capacity, and higher rate capabilities, better reversibility, and a more stable cycling performance were confirmed on the turbostratic microstructure. First-principles calculations suggest that the multitudinous lattice domains of the T-GNSs contain diverse intercalation sites with strong binding energies, which could be the origin of the high-performance solid-solution potassium-ion intercalation behavior when the turbostratic graphene stacks have a *d*-spacing smaller than that of equilibrium potassium–graphite intercalation compounds (5.35 Å).

1. Introduction

Potassium-ion batteries (PIBs) have received considerable attention as an alternative to lithium-ion batteries (LIBs) as a power source because of the approximately 1000 and 100 times larger potassium resources in Earth's crust and oceans, respectively, and lower electrode potential in organic electrolyte systems [1–5]. In addition, the larger alkali cation with lower Lewis acidity has a higher ionic conductivity, lower stoke radius, and lower desolvation energy, possessing superior theoretical rate capabilities [6,7]. Moreover, potassium-ion intercalation into carbon-based anode materials (CAMs) is attractive from a commercial point of view because mass-produced and well-established CAMs, which led to the commercial success of LIBs, can be used as active anode materials [8]. Stable phase reactions forming KC_8, KC_{24}, KC_{36}, and KC_{48} have been identified for potassium–graphite intercalation compounds, indicating that large-sized potassium ions (four coordinated, tetrahedral, ~1.51 Å) can be inserted in every graphene sheet [9,10]. However, the KC_8 phase requires a huge volume expansion of the graphene lattice of up to 5.35 Å, corresponding to ~ 160% to the initial lattice spacing. Repeated expansion/contraction during charging/discharging consecutively deconstructs the solid–electrolyte interface layers, leading to continuous electrolyte decomposition and an increase in surface film resistance [11–13]. In addition, the theoretical capacity of KC_8 in a graphite anode (~279 mA h g^{-1}) is considerably lower than that of LiC_6 (372 mA h g^{-1}). Moreover, the theoretical potassium-ion intercalation capacity is difficult to achieve in practice owing to the sluggish solid-state diffusion rate of potassium-ion charge carriers in the host graphitic lattices [14].

As alternative potassium–graphite intercalation compounds, functionalized carbons and/or porous carbons with short-range

* Corresponding authors.
E-mail addresses: hjjin@inha.ac.kr (H.-J. Jin), hklim@kangwon.ac.kr (H.-K. Lim), c-ysyun@korea.ac.kr (Y.S. Yun).

https://doi.org/10.1016/j.jechem.2021.11.027

graphitic ordering have been actively reported because the large number of redox centers, such as functional groups and topological defects, in these materials can store charges very quickly through surface-driven Faradaic reactions [15–31]. Pseudocapacitive reactions are remarkably fast and stable, leading to high power capabilities and long cycle lives. However, the surface-induced solid-solution reactions are accompanied by a continuous voltage drop with potassiation, resulting in insufficient energy performance [16,17]. The conflicting energy and power characteristics between ordered graphite and amorphous carbon materials clearly indicate that neither carbon material is suitable as an anode for PIBs. Hence, further research is required to develop high-performance CAMs that have higher specific energies and powers than those of graphite but with more stable and longer cycling lifespans.

Herein, we report the solid-solution potassium-ion intercalation behavior of multilayered turbostratic graphene nanosheets (T-GNSs) with disordered local carbon microstructures. Unlike the general belief that a solid-solution reaction is accompanied by a voltage change, the T-GNSs showed a plateau-like voltage capacity at low voltages (~0.5 V) through potassium-ion intercalation reactions in the turbostratic graphitic lattices (3.65–4.18 Å). In addition, the plateau voltage capacity (~200 mA h g^{-1}) of the T-GNSs was considerably higher than that (~120 mA h g^{-1}) of well-ordered graphite nanoplates (GNPs, XGnP graphene nanoplatelets, Grade M, XGSciences, US). Moreover, the solid-solution potassium-ion intercalation reaction showed a higher sloping capacity, a higher rate capability, better reversibility, and more stable cycling performance. First-principles calculations revealed that the unusual potassium-ion storage behavior originates from the effects of defective sites in the stacked graphene basal planes of T-GNSs, which cause the electronic structure to have more metallic characteristics. This enhances the electron affinity of the defective graphene surface, leading to a higher potassium-ion storage capacity and faster and more stable potassium-ion adsorption behavior in a nearly monovalent state compared with those of well-ordered graphite materials.

2. Experimental

2.1. Preparation of T-GNSs

A commercial graphene oxide dispersion (1 wt%, JGO-25, JMC, South Korea) was lyophilized at −50 °C under ~ 5 Pa for 3 days, and the resulting graphene oxide powder was heated at 800 °C for 2 h in a tube furnace under Ar flow of 300 mL min^{-1}. A heating rate of 5 °C min^{-1} and natural cooling were applied for the heating process. The product T-GNS powders were then stored in a vacuum oven at 30 °C.

2.2. Characterization

The material properties of the T-GNSs and GNPs were characterized by scanning electron microscopy (SEM, S-4300, Hitachi, Japan), transmission electron microscopy (TEM, JEM2100F, JEOL, Japan), X-ray diffraction (XRD, Rigaku D/MAX 2500, Rigaku, Japan), Raman spectroscopy (514.5 nm, 2.41 eV, 16 mW), X-ray photoelectron spectroscopy (XPS, PHI 5700 ESCA, USA), and nitrogen adsorption/desorption isotherms (ASAP 2020, Micromeritics, USA). Electrochemical tests were conducted using 2032-type coin cells and automatic battery cyclers (WBCS3000, Wonatech, Korea). The working electrodes were prepared using a slurry method in which 90 wt% of T-GNSs or GNPs was mixed with 10 wt% of a polyvinylidene fluoride (PVDF, Sigma-Aldrich, USA) binder in an N-methyl-2-pyrrolidone solution and then homogeneously coated on a Cu foil (20 μm, Welcos, Korea) through bar coating. The electrodes (1/2 inch in diameter) were punched, where the active material loading density was controlled at ~ 1 mg cm^{-2} for each electrode. The coin cells were assembled in a glovebox filled with argon gas using T-GNSs or GNPs as the working electrode and potassium metal (~99.5%, Sigma-Aldrich, USA) as both the reference and counter electrodes. A glass microfiber filter (GF/F, Whatman, US) was used as the separator.

2.3. Computational method

First-principles density functional theory (DFT) calculations were performed using the Vienna ab initio simulation package (VASP) [32,33]. The electron–ion interaction was described by the projector augmented wave (PAW) [34] method with a plane-wave energy of up to 400 eV. The vdW-DF [35] exchange–correlation functional was used to adequately describe the van der Waals interactions. All bulk and surface models were generated based on 6 × 6 supercells composed of hexagonal graphite unit cells. The integration in k-space was performed with 2 × 2 × 5 and 2 × 2 × 3 Monkhorst–Pack grids for graphite and potassium-intercalated structures, respectively. All surface models included a 15 Å vacuum region along the surface normal direction. The Methfessel–Paxton smearing method was used to determine electron occupations with a smearing energy of 0.2 eV. The optimized geometries were obtained with criteria of atomic forces less than 0.01 eV $Å^{-1}$ and a total energy convergence of less than 10^{-5} eV. The intercalation potential between compositions x_2 and x_1 of the potassiated graphite was calculated as follows:

$$V \approx -\frac{E(K_{x_1}C_8) - E(K_{x_2}C_8) - (x_1 - x_2)E(K_{\text{metal}})}{(x_1 - x_2)}$$

where K_{metal} is the body-centered cubic potassium bulk phase. Bader partial charge analysis was performed using a code provided by the Henkelman group [36].

3. Results and discussion

The two-dimensional (2D) morphologies of the T-GNSs with large-area lateral sizes were observed by SEM and TEM (Fig. 1a, b, and f respectively). The lateral dimensions of the T-GNSs were several tens of micrometers, which were approximately five times larger than those (a few micrometers) of the GNPs (Fig. 1e and f). Further information for the morphologies of both samples can be confirmed in the low magnification SEM images as shown in Fig. S1. In addition, high-resolution TEM (HR-TEM) images showed a glaring contrast in their graphitic microstructures (Fig. 1c and g, and Fig. S2). The HR-TEM image of the T-GNSs exhibited a turbostratic graphitic structure with a large variation in *d*-spacing, while that of the GNPs represented a well-ordered graphitic structure with a relatively uniform lattice spacing. The specific *d*-spacing variations are depicted as frequency distribution bar graphs, which were obtained from HR-TEM images by calculating the lattice distances of more than 100 samples (Fig. 1d and h). The *d*-spacings of the T-GNSs and GNPs ranged primarily between 3.65 and 4.18 Å and between 3.34 and 3.46 Å, respectively, indicating that the T-GNSs had larger and a considerably broader range of *d*-spacings. The selective area diffraction (SAD) patterns support the prominent crystallographic differences (insets in Fig. 1c and g). The SAD pattern of the T-GNSs exhibited a blurred ring pattern, indicating an amorphous microstructure. In contrast, many clear points from well-ordered (002) and (100) graphite structures were observed for the GNPs. The larger and broader range of *d*-spacings in the graphitic structure are induced from intrinsic/extrinsic defects which have sp^3-hybridized carbon bonds in the poly-hexagonal carbon plane [37,38]. The stereoscopic sp^3-hybridized

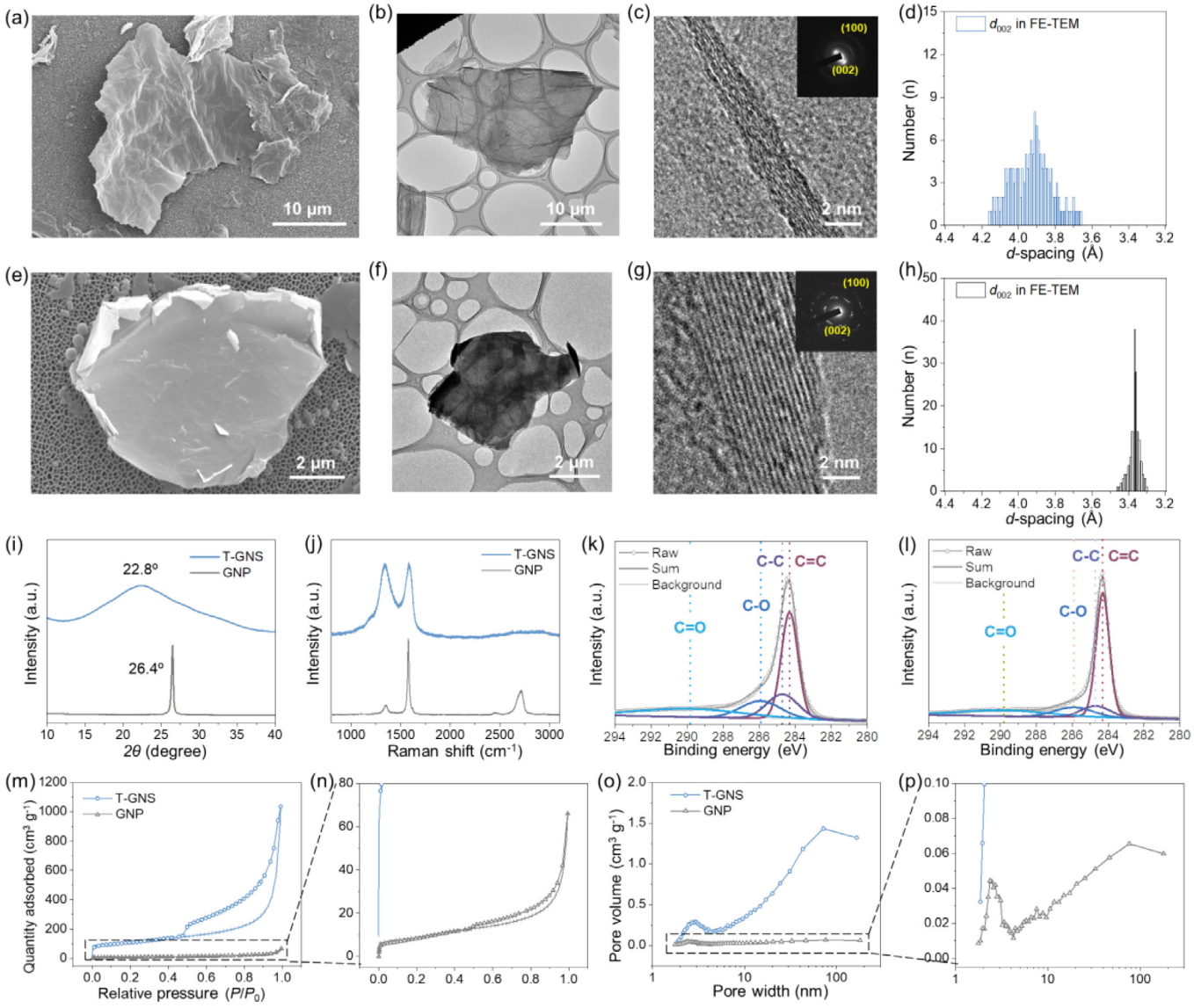

Fig. 1. Material properties of the T-GNSs and GNPs. (a) SEM, (b) TEM, and (c) HR-TEM images (inset shows SAD pattern) and (d) *d*-spacing variation data obtained from HR-TEM images of the T-GNSs. (e) SEM, (f) TEM, and (g) HR-TEM images (inset shows SAD pattern) and (h) *d*-spacing variation data obtained from HR-TEM images of the GNPs. (i) XRD patterns and (j) Raman spectra of the T-GNSs and GNPs. XPS C 1*s* spectra of the (k) T-GNSs and (l) GNPs. (m and n) Nitrogen adsorption/desorption isotherms of the T-GNSs and GNPs depicted with different nitrogen adsorption ranges, and (o and p) pore-size distribution data of the T-GNSs and GNPs depicted with different pore volume ranges.

carbons in the graphene plane deform the planar carbon sheets into twisted and tortuous shapes, leading to poorly stacked graphitic structures.

The microstructural differences were further investigated using XRD and Raman spectroscopy (Fig. 1i and j, respectively). In the XRD pattern of the T-GNSs, a very broad graphite (002) peak centered at 22.8° was confirmed, which coincides with the broad range of lattice spacings found in the TEM observations. The average *d*-spacing of the expanded lattices was calculated to be ~ 3.90 Å (Fig. 1i). In contrast, the XRD pattern of the GNPs exhibited a relatively sharp graphite (002) peak at 26.4° (*d*-spacing: 3.38 Å), which is very close to the typical graphite structure (Fig. 1i). The crystalline graphitic domain sizes (L_c) of the T-GNSs and GNPs were calculated to be 2.3 and 29.4 nm, respectively, from the XRD patterns using to the Scherrer equation [37]. Note that the ordered graphitic domain size of the GNPs was ~ 13 times larger than that of the T-GNSs in spite of the substantially smaller contour particle sizes. In the Raman spectra, the signature *D* and *G* bands of aromatic polyhexagonal carbon rings were detected at ~ 1350 and ~ 1582 cm^{-1} for the GNPs and at ~ 1345 and ~ 1582 cm^{-1} for the T-GNSs (Fig. 1j). The redshift of ~ 5 cm^{-1} in the *D* band of the T-GNSs indicates that the polyhexagonal structures were slightly distorted by tensile strain [39]. The integrated areal intensity ratios (I_D/I_G) of the T-GNSs and GNPs were ~ 1.59 and ~ 0.31, respectively, and their graphenic domain sizes (L_a) were calculated to be ~ 10.6 and 54.3 nm, respectively (Fig. S3) [40]. In addition, the Raman spectrum of the GNPs displayed a distinctive 2D band, which indicates a three-dimensional ordering of the graphene sheets. This is in contrast to that of the T-GNSs, which did not have a 2D band (Fig. 1j). From the HR-TEM, XRD, and Raman spectroscopy analyses, it was confirmed that the T-GNSs had a turbostratic graphite structure composed of nanometer-scale crystalline domains and expanded graphitic lattices with a broad range of *d*-spacing.

The surface properties of the T-GNSs and GNPs were characterized by XPS, as shown in Fig. 1(k and l), respectively. The C 1 *s* spec-

tra revealed that both samples were composed primarily of sp^2-hybridized carbon–carbon double-bond structures (284.4 eV) with a small proportion of sp^3-hybridized carbon–carbon single-bond configurations (284.7 eV). The T-GNSs had a higher proportion of sp^3-hybridized carbon, which originated from intrinsic defects such as Stone–Wales, mono-vacancy, di-vacancy, pseudo-edge, and edge defects. In addition, the C 1 *s* spectrum of the T-GNSs displayed a higher intensity of carbon–oxygen single-bond configurations, indicating the presence of more oxygen heteroatoms (Fig. 1k and l). The O 1 *s* spectrum of the T-GNSs also shows the higher intensity of carbon–oxygen single-bond configuration (Fig. S4a). In contrast, the O 1 *s* spectrum of the GNPs reveals that a carbon–oxygen double bond structure is their main configuration (Fig. S4b). The O/C ratio of the T-GNSs was ~ 0.073, which is ~ 2 times higher than that of the GNPs (~0.036). The XPS survey spectra support that the T-GNSs are mainly composed of carbon and oxygen bonds (Fig. S5).

To characterize the specific open surface areas of the T-GNSs and GNPs, nitrogen adsorption/desorption isotherm tests were conducted (Fig. 1m-p). The isotherms of both samples exhibited typical IUPAC classification type-IV behavior (mesoporous structures) with type-H2 hysteresis loops, which implies that the pores were slit-shaped (Fig. 1m and n). The pore-size distributions of both samples had similar shapes with a broad range of pore sizes from mesopores to macropores, although there was a large difference in the magnitudes of the pore volumes (Fig. 1o and p). The specific surface area (~370 $m^2\ g^{-1}$) of the T-GNSs was ~ 12 times higher than that of the GNPs (~31 $m^2\ g^{-1}$). It is worth noting that the large gap in the quantity of adsorbed nitrogen was considerably more dependent on the local microstructure, such as L_a and L_c, than on the macroscopic sheet size. This means that more nitrogen molecules can permeate into the interior of the defective carbon structures, where the inner surfaces of the multitudinous carbon basic structural units can be exposed as open surfaces. Considering that the kinetic diameter of nitrogen molecules is ~ 3.64 Å, substantially smaller alkali cations can be more easily inserted along the large open surfaces, which is advantageous for the charge transport rate inside the T-GNSs.

The alkali cation storage behaviors in the different carbon microstructures of the T-GNSs and GNPs were investigated by comparing their potassium-ion and lithium-ion storage behaviors in KPF_6 and $LiPF_6$ electrolyte systems, respectively, dissolved in an ethylene carbonate (EC) and dimethyl carbonate (DMC) (1:1 v/v) mixed solution. Cyclic voltammetry (CV) tests were conducted between 0.01 and 3.0 V (Fig. 2a and 2b). In lithium-ion half-cells, a sharp reduction/oxidation peak pair was observed in the low-voltage region (~0.01/~0.23 V) of the CV curve of the GNPs, while no oxidation peak was evident in the CV curve of the T-GNSs, indicating that the lithium-ion intercalation reaction is highly affected by the local graphitic structure (Fig. 2a). Numerous studies support carbon-microstructure-dependent lithium-ion storage behavior [41–43]. However, in potassium-ion half-cells, clear redox peak pairs at ~ 0.4 and ~ 0.5 V were confirmed in the CV curves of the GNPs and T-GNSs, respectively (Fig. 2b). The reversible oxidation peaks in the low-voltage region reveal that similar potassium-ion intercalation reactions occur in both well-ordered and turbostratic graphite structures, which clearly differs from the lithium-ion storage behavior of the T-GNSs. Another noteworthy observation is the substantially larger electrochemically active surface areas (ECSAs) of the T-GNSs in both lithium-ion and potassium-ion cells than those of the GNPs (Fig. 2a and b). Particularly for the potassium-ion cells, the CV curve of the T-GNSs had a higher integral curve area as well as a strong area redox peak pair, implying that the potassium-ion intercalation reaction occurs with a large number of pseudocapacitive charge storage reactions (Fig. 2b) [44]. The pseudocapacitance was quantitatively fit using the CV curves of the T-GNSs at different scan rates (Fig. S6). The pseudocapacitive contribution gradually increased with increasing scan rate, with pseudocapacitance ratios of ~ 22%, ~43%, ~52%, ~64%, ~74% and 79% at scan rates of 0.1, 0.2, 0.5, 1, 2, and 5 mV s^{-1}, respectively. The distinctive charge storage behaviors of the T-GNSs were further studied through galvanostatic discharge/charge tests at a current density of 25 mA g^{-1} (Fig. 2c and d). In lithium-ion half-cells, the galvanostatic charge (delithiation) profile of the GNPs exhibited a reversible plateau voltage capacity of ~ 210 mA h g^{-1} at ~ 0.1 V, followed by a sloping voltage capacity of ~ 140 mA h g^{-1}; this is quite different from that of the T-GNSs, which did not demonstrate a noticeable plateau voltage capacity (Fig. 2c). The overall reversible capacities of the T-GNSs were considerably higher (~580 mA h g^{-1}), and most of the capacities were obtained with a continuous voltage increase. Hence, the T-GNSs primarily stored lithium ions via a solid-solution reaction mechanism. However, in the potassium-ion cells, the galvanostatic charge profiles of both the GNPs and T-GNSs exhibited similar plateau-like low-voltage capacities of ~ 120 and ~ 200 mA h g^{-1} at ~ 0.5 V, respectively, where the T-GNSs presented a higher plateau voltage capacity, despite their poor graphitic ordering. Moreover, the T-GNSs exhibited a substantially higher sloping voltage capacity (~220 mA h g^{-1}) in a higher voltage range (>0.7 V). These results indicate that the T-GNSs had more redox-active sites for both intercalation and pseudocapacitive reactions. Essentially, the pseudocapacitive alkali cation storage reaction occurs by chemisorption of the charge carriers on the defective sites of the graphene planes, such as edge defects, extrinsic defects, and topological defects. Because the *d*-spacings of the T-GNSs were larger than the equilibrium *d*-spacing (3.70 Å) of lithium–graphite intercalation compounds, the lithiation reaction on the T-GNSs could mainly occur along a single graphene surface by surface-driven redox reactions rather than by intercalation reactions between two graphene layers [45,46]. The pseudocapacitive reaction on a single graphene surface can store more charges than that of the intercalation reaction. However, the binding energy with alkali cations could be higher on the single graphene layer than that between two graphene layers, leading to a higher redox voltage of the pseudocapacitive alkali cation storage reaction. Therefore, the lithiation/delithiation profiles of the T-GNSs with the larger *d*-spacings resulted from the pseudocapacitive reactions with higher specific capacities (~580 mA h g^{-1}), while those of the GNPs composed of well-ordered graphitic lattices mainly originated from intercalation-based plateau voltage capacities (~210 mA h g^{-1} at ~ 0.1 V). However, the expanded graphitic lattices of the T-GNSs were still smaller than the equilibrium slab distance (5.35 Å) of the potassium–graphite intercalation compounds, wherein potassium-ion intercalation reactions could mainly occur for both the T-GNSs and GNPs. Therefore, it is reasonable that they exhibited similar potassium-ion intercalation behaviors in the low-voltage region. However, the higher plateau-like voltage capacity of the T-GNSs requires further consideration because the presence of topological defects on the graphene basal plane creates a strain on the neighboring six-membered rings and even more remote ring structures, leading to large defective domains. Therefore, the origin of the higher plateau capacity of the T-GNSs was further investigated by first-principles calculations, which will be discussed in the following section.

More detailed potassium-ion storage mechanisms of both samples were characterized using the redox peak currents in the CV curves obtained at different sweep rates (Fig. 2e and S7). The peak currents increase with the sweep rate according to a power law relationship: $i = av^b$, where a and b are adjustable values [47]. A diffusion-controlled charge storage mechanism has a b value of ~ 0.5, which increases to ~ 1 when a surface-controlled reaction mechanism is dominant. Based on the oxidation peak currents of

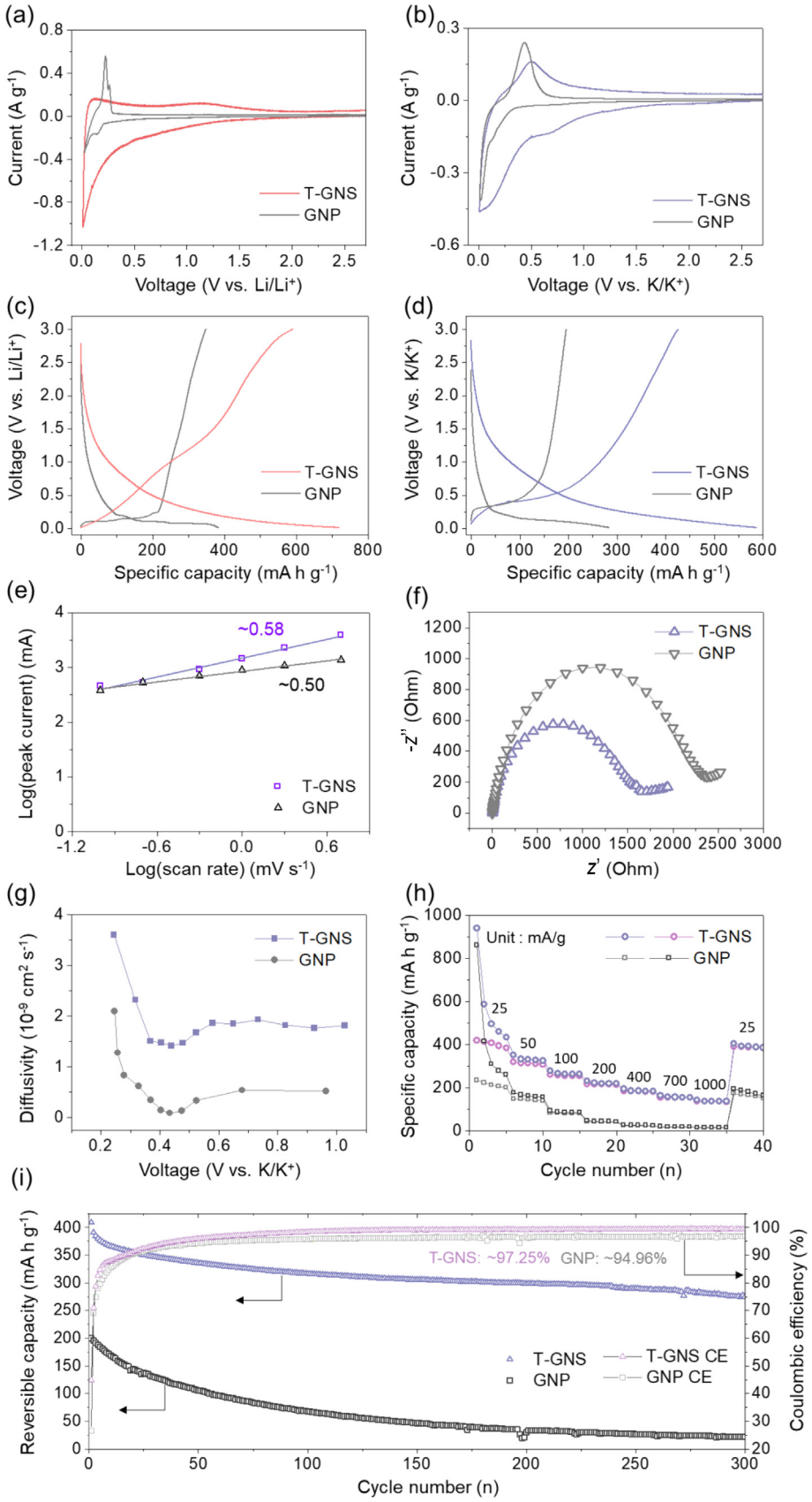

Fig. 2. Electrochemical performances of the T-GNSs and GNPs in $LiPF_6$ and KPF_6 electrolytes dissolved in an EC/DMC mixed solution over a voltage window of 0.01 to 3.0 V vs. Li^+/Li and K^+/K, respectively. Cyclic voltammograms of (a) lithium-ion and (b) potassium-ion cells at a scan rate of 0.1 mV. Galvanostatic discharge/charge profiles of (c) lithium-ion and (d) potassium-ion cells at a current rate of 25 mA g^{-1}. (e) Specific peak currents of cyclic voltammograms at different scan rates, (f) EIS profiles at frequencies between 50 mHz and 1 MHz after potassiation at 0.01 V, (g) variations in potassium-ion diffusivity values with voltage, (h) rate capabilities at current densities from 25 to 1000 mA g^{-1} (followed by reversible rate capability at 25 mA g^{-1}), and (i) cycling performances with Coulombic efficiency values over 300 cycles of the T-GNSs and GNPs in potassium-ion cells.

the GNPs and T-GNSs in the CV curves of the potassium-ion systems, the *b* values were ~ 0.50 and 0.58, respectively. This reveals that the potassiation behavior in the turbostratic structure progressed with a partly surface-controlled reaction, which is advantageous for the potassium-ion transport kinetics. Electrochemical impedance spectroscopy (EIS) data collected at frequencies between 50 mHz and 1 MHz after potassiation at 0.01 V support the facile charge delivery on the T-GNSs (Fig. 2f). The EIS profiles of the GNPs and T-GNSs exhibited one large semicircle corresponding to 2,400 and 1,700 Ω, respectively, where the semicircle was induced by both the surface film resistance (R_f) and charge transfer resistance (R_{ct}). The smaller semicircle of the T-GNSs indicates more favorable charge-delivery kinetics. Additionally, potassium-ion diffusivity was calculated using the galvanostatic intermittent titration technique at a current rate of 25 mA g^{-1} with a rest time of 2 h (Fig. S8) [48]. The potassium-ion diffusivity values (1.4–3.6 × 10^{-9} cm^{-2} s^{-1}) in the T-GNSs were approximately 2–10 times higher than those in the GNPs (0.1–2.1 × 10^{-9} cm^{-2} s^{-1}) at all the tested voltage ranges, which coincides with the results from the power law and EIS analyses (Fig. 2g). The lower charge transfer resistance and higher potassium-ion diffusivity led to higher rate capabilities for the T-GNSs. At the tested current densities (which were increased from 25 to 1000 mA g^{-1} in stages), the initial capacity gap gradually increased with increasing current density (Fig. 2h). When the current density reached 200 mA g^{-1}, the reversible capacities of the GNPs were reduced to < 50 mA h g^{-1}, while those of the T-GNSs were ~ 220 mA h g^{-1}. In addition, when the current density was returned to its initial value after 35 cycles, the T-GNSs retained high reversible capacities of ~ 390 mA h g^{-1}, corresponding to the atomic ratio $KC_{5.7}$, whereas the GNPs showed relatively poor capacities of ~ 170 mA h g^{-1} ($KC_{13.1}$) and a gradual reduction in capacity (Fig. 2h). The superiority of the T-GNSs can be further confirmed through comparison with previously reported carbon-based anode materials (Table S1). Additionally, the potassium-ion storage performances of the GNPs and T-GNSs were compared after doubling the mass-loading density (~2 mg cm^{-2}, Fig. S9). In the galvanostatic profiles, the reversible capacities of both the T-GNSs and GNPs were reduced in the higher mass-loading density condition. However, the capacity reduction of the T-GNSs (~15%) was substantially smaller than that of the GNPs (~23%), indicating the T-GNS electrode has better kinetic performance under the same conditions. Hence, the T-GNSs exhibited a better rate performance and reversibility for potassium-ion storage. The cycling performances of the T-GNSs and GNPs were tested at a current rate of 25 mA g^{-1} for the potassium-ion cells (Fig. 2i). The T-GNSs exhibited stable cycling behavior, where reversible capacities of ~ 275 mA h g^{-1} were maintained after 300 cycles. In contrast, the GNPs exhibited a continuous large capacity drop from the initial cycle, with reversible capacities reaching half the initial value after 150 cycles. After 300 cycles, the reversible capacities of the GNPs were below 30 mA h g^{-1}, showing poor cycling performance. The initial Coulombic efficiency (CE) of the T-GNSs was ~ 45%, which was much higher than that of the GNPs (~27%). The CE values of the T-GNSs and GNPs gradually increased with increasing number of cycles to ~ 97.25% and 94.96%, respectively. The stark differences in the cycling performances can also be observed in the galvanostatic profiles at different cycles (Fig. S10). The cycling performances of the T-GNSs were further tested under high rate conditions. A reversible capacity of > 100 mA h g^{-1} was maintained by 500 mA g^{-1} after 200 cycles, demonstrating good cycling performance (Fig. S11).

To clarify the potassium-ion storage mechanisms of the GNPs and T-GNSs, ex situ Raman analysis was conducted at different states of charge (SoCs) during the galvanostatic charge/discharge processes (Fig. 3a and b). In a previous study on graphite foam, splitting of the *G* band in the Raman spectra was observed, which was thought to be induced by the separation of local graphenic carbon structures into two phases, the potassium-ion-intercalated phase and the neighboring phase with no potassium ions [49]. The occurrence of a new *G* band with potassium-ion intercalation can be confirmed in the higher frequency region, indicating that the in-plane carbon–carbon bond length in the intercalated phase is shortened by strong interaction with the intercalated potassium ions. Herein, *G* band separation occurred in the ex situ Raman spectra of the GNPs during the potassiation process, where the high-frequency *G* band intensity gradually increased with increasing plateau voltage capacity, indicating that potassium ions were stored by a two-phase intercalation reaction (Fig. 3a). In the subsequent depotassiation process, the high-frequency *G* band intensity gradually decreased with decreasing SoC, and finally, the initial *G* band was restored to its original shape. Contrary to the ex situ Raman spectra of the GNPs, a new high-frequency *G* band was not formed during the potassiation/depotassiation processes of the T-GNSs (Fig. 3b). One noteworthy result is the gradual red shift of the *G* band with increasing SoC for the T-GNSs, where the peak centered at ~ 1580 cm^{-1} shifted to a minimum value of ~ 1560 cm^{-1} in the fully potassiated state. The progressive red shift indicates that a solid-solution potassium-ion intercalation reaction occurred, which caused continuous extension of the in-plane carbon–carbon bond length in local carbon domains. This is a completely different reaction mechanism from the blue-shifted phase formation reaction of the GNPs. Nevertheless, the galvanostatic charge/discharge curves showed a plateau-like voltage profile in the low-voltage region (~0.5 V). In addition, the overall specific capacities of the T-GNSs (~420 mA h g^{-1}) were ~ 2 times higher than those of the GNPs (~200 mA h g^{-1}); the T-GNSs exhibited a ~ 60% higher plateau-like capacity at ~ 0.5 V (Fig. 2d).

The schematics in Fig. 3(c), illustrate the relationship between the potassium-ion intercalation reaction and the voltage profile of the GNPs. The α and β phases represent the carbon domains without and with intercalated potassium ions, respectively, where the chemical potential (μ) in the long-range two-phase region is fixed at the same value, and accordingly, the main plateau voltage capacity occurs during the potassiation process. In contrast to the typical two-phase potassium-ion intercalation reaction of the GNPs, $\Delta\mu$ of the KC_x phase continuously decreases with potassiation for the T-GNSs (Fig. 3d). Note that $\Delta\mu$ of the T-GNSs is gradually mitigated with increasing SoC, and a nearly plateau-like voltage profile is exhibited at higher SoCs (Fig. 3d). The slight change in $\Delta\mu$ is due to the presence of numerous redox active sites, which have similar energy states. Because the potassiation reaction progresses successively along the reaction pathway via active sites with the lowest $\Delta\mu$, the plateau-like voltage profile can indicate when T-GNSs have a large number of redox centers in the low voltage region. More explanation for the Fig. 3(c and d) was exhibited in Fig. S12.

The first-principles calculation results support our claim that T-GNSs can deliver considerably higher energy and power densities than those of GNP via the solid-solution potassium-ion intercalation reaction mechanism with a pseudo-plateau voltage capacity (Fig. 4). To create a simplified model of the experimental T-GNS material (in which various defects were combined), three defective graphite models were generated by stacking the graphene layers with V_2 defects (i.e., 585, 555–777, and 5555–6-7777) in an AB sequence (Fig. 4a). The intercalation potentials of potassium ions for perfect and defective graphite structures were calculated using DFT. For perfect graphite, three intercalated structures, KC_{24}, KC_{16}, and KC_8 (as reported in previous studies), were selected.[8] In defective graphite with the same compositional structure as potassium-intercalated perfect graphite, the interaction energy between the

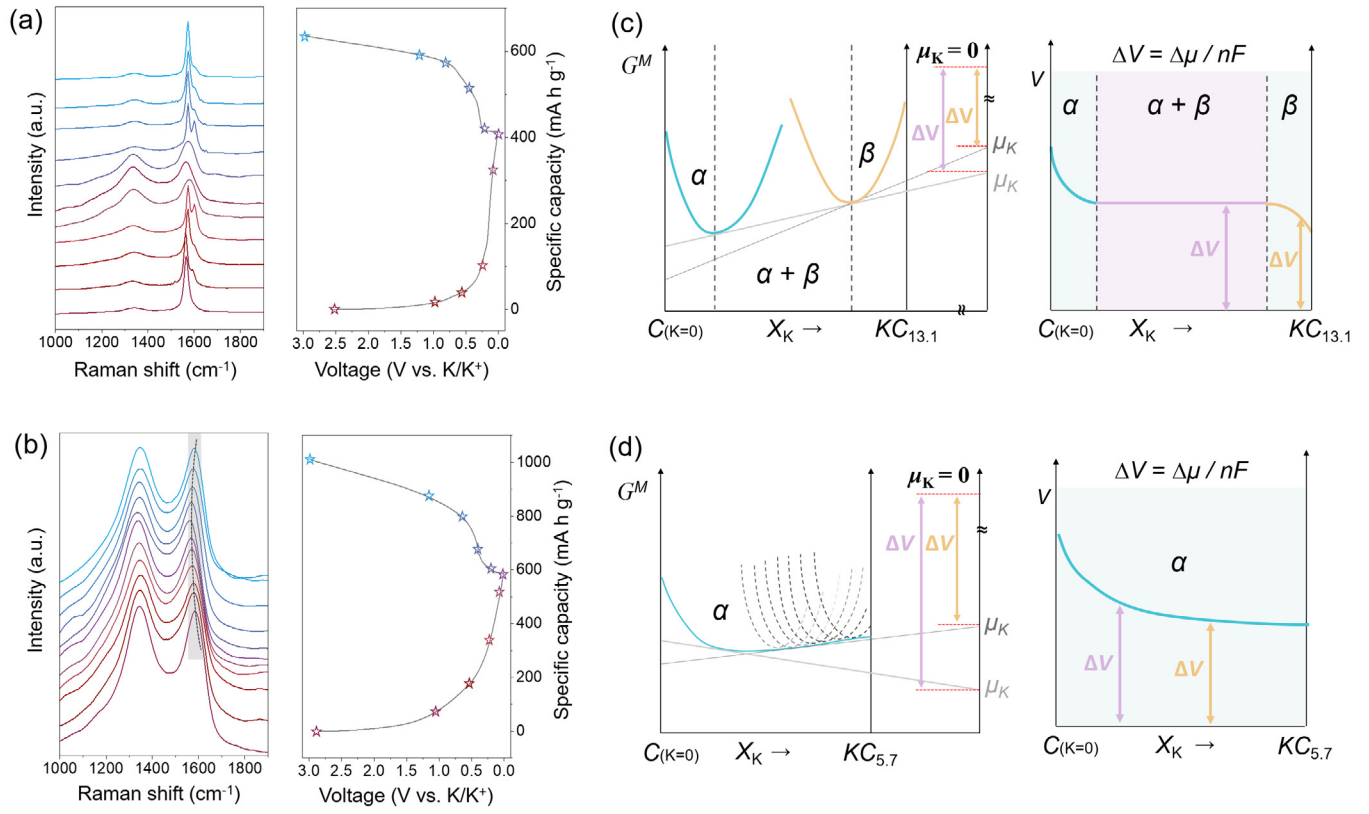

Fig. 3. Ex situ Raman spectra of the (a) GNPs and (b) T-GNSs. Schematics showing $\Delta\mu$ of the (c) GNPs and (d) T-GNSs with potassiation and corresponding changes in the voltage profiles.

potassium and defective graphene layer varies depending on the arrangement of the potassium ion. Therefore, in this study, two different laterally translated potassium-ion intercalation structures were calculated (Fig. S13) for each defective graphite model (i.e., a total of six structures for each stage). The average intercalation potentials and their deviations are shown in Fig. 4(b). For the defective graphite, the average potential of each composition was higher than that of the perfect graphite in all stages, which is consistent with the experimental voltage profiles. The potential difference was largest in the first stage (KC_{24}) and decreased with increasing SoC, similar to the experimental results. The potential deviation of the defective graphite model was quite large depending on the arrangement of the potassium ion and defect structure, which indicates that the experimental voltage profile represents the solid-solution behavior. In addition, the higher potential compared to that of the perfect graphite indicates that the reduction of potassium ions in the defective graphite host structure is easier than that in perfect graphite.

To determine the origin of the different potential behaviors, the potassium atom binding energies were calculated for the perfect graphene and V_2 defective graphene surfaces (Fig. S14). The potassium binding energies based on the various ring structures present on the graphene surfaces are shown in Fig. 4(c). The binding energy for perfect graphene was −0.11 eV, which is weak (physisorption level). In contrast, the binding energies for the C_5-C_8 rings present in the defect regions were between −0.54 and −1.31 eV, which were approximately 5 to 13 times stronger than that of perfect graphene. These calculation results explain why a defective graphite material (e.g., the T-GNSs in the experiment) can be charged at a higher potential than that of a perfect graphite material (e.g., the GNPs in the experiment): the intrinsically strengthened interaction between potassium and the defective carbonaceous surface is reflected in the intercalation structure. This also means that potassium ions can be easily reduced on the surface of defective graphite, which most likely explains the origin of the relatively long sloping voltage profile in the initial potassiation stage of the T-GNSs.

Interestingly, the binding energy tended to decrease as the distance between the C_6 binding site and the defect region increased. However, it was still considerably stronger (>-0.71 eV) than that of the perfect graphene. This is because the electronic structure of the basal plane is affected by the defect site. The density of states (DOS) and the atomic partial charge of potassium were analyzed to identify the origin of this behavior. As shown in Fig. 4(d), the DOS near the Fermi level of each defective graphene model showed a higher state density than that of the perfect graphene, which is consistent with previous studies [50–54]. Thus, defective graphene has more metallic characteristics than perfect graphene, thereby facilitating potassium-ion reduction because of the improved electrical conductivity. Furthermore, as shown in Fig. 4(e), the partial charge of the potassium atom adsorbed on the defective graphene models had a higher oxidation state (+0.88 to + 0.91) than that of the perfect graphene (+0.79). This indicates that the increased DOS near the Fermi level enhanced the electron affinity of the defective graphene surface, which enabled the adsorption of potassium into a nearly stable monovalent state, resulting in a stronger binding energy. These calculation results clarify that the surface and lattice domains of the T-GNSs contain various intercalation sites with strong binding energies, which are the origin of the solid-solution potassium-ion intercalation behavior.

DFT calculations also identified the origin of the pseudo-plateau voltage profile of the T-GNSs during potassiation compared to the solid-solution behavior during lithiation. Because the T-GNSs had an expanded *d*-spacing with a broader distribution compared to

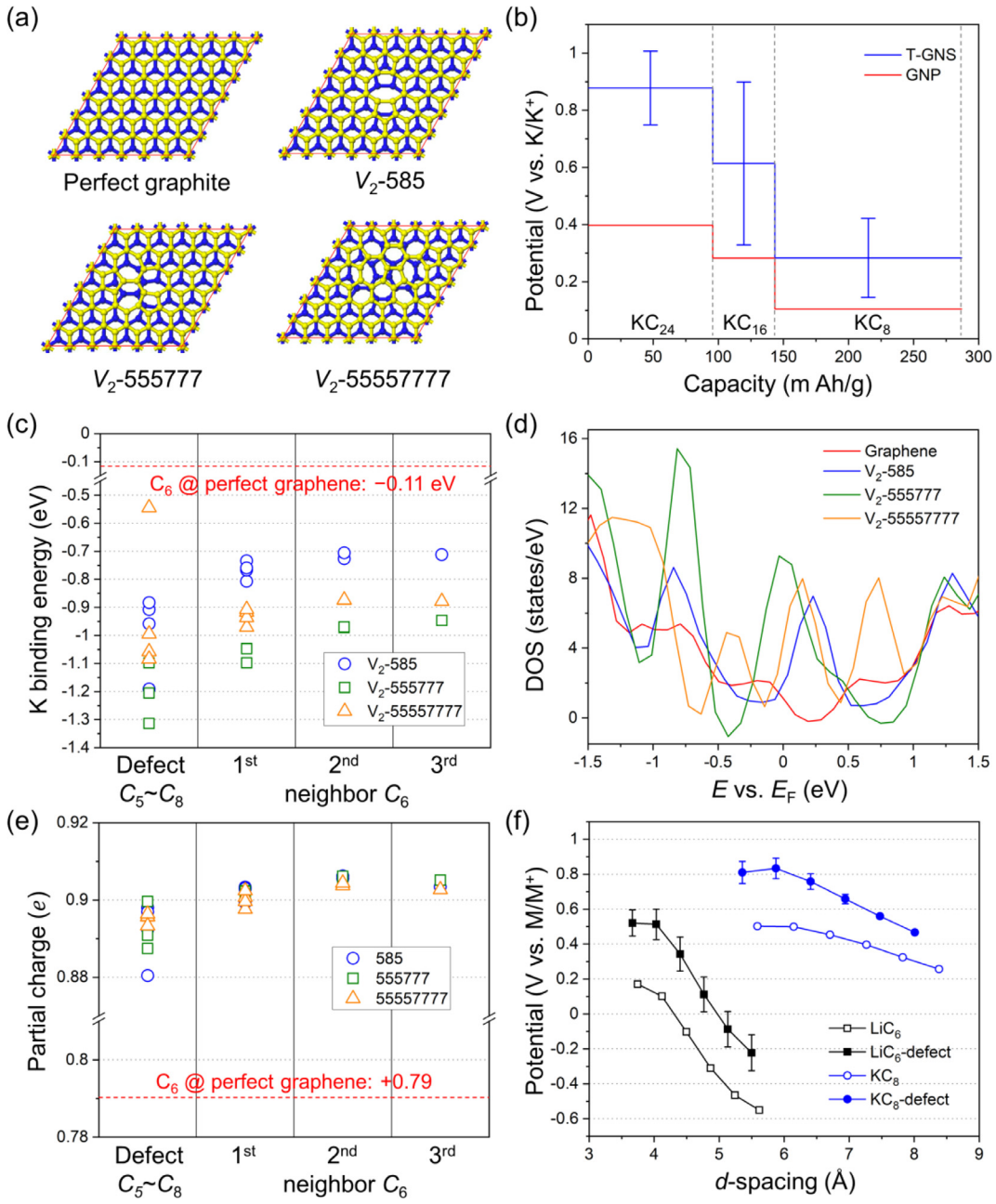

Fig. 4. First-principles calculation data. (a) Structure models for perfect and defective graphite materials. Defective graphite composed of di-vacancy (V_2) 585, 555777, and 55,557,777 graphene sheets with an AB stacking sequence. (b) Theoretical voltage profiles for KC_{24}, KC_{16}, and KC_8 compositions based on perfect and defective graphite structures. The average and standard deviation of the calculated voltage values were plotted for the T-GNSs. (c) Potassium binding energies on perfect and defective graphene surfaces. (d) Density of states near the Fermi level for perfect and defective graphene models. (e) Partial charges of a potassium atom in the adsorbed state calculated using Bader analysis. (f) Variation in the intercalation potentials of Li^+ and K^+ with the *d*-spacing for perfect and defective graphite structures.

that of perfect graphite, the intercalation behavior of lithium and potassium ions could be differentiated by dissimilar interactions between cations and graphite interlayers. The intercalation potentials were calculated for fully intercalated LiC_6 and KC_8 structures with *d*-spacings that were 10%-50% larger than that of the equilibrium lattice (Fig. 4f). As the *d*-spacing increased, the thermodynamic stability of the ions in the graphite interlayer decreased, which caused the intercalation potential to decrease. Intercalation in the defective graphite occurred at a higher potential for both ions than that of the perfect graphite because of the relatively strong ion–graphene binding energy, as discussed previously. It is worth noting that the degree of instability resulting from the *d*-spacing expansion was more significant in the lithiation cases than in the potassiation cases. The lithiation potential decreased to below the Li metal reduction potential when the *d*-spacing was increased by more than 20% for perfect graphite and 40% for defective graphite. Considering the broad *d*-spacing distribution of the T-GNSs, only a part of the lattice domains could have an optimal *d*-spacing for homogeneous lithiation. Thus, in the rest of the domains, lithium intercalation involved lattice contraction processes, which have extensive thermodynamic costs. For this reason, the lithiation of the T-GNSs showed a solid-solution voltage profile, as shown in the experiments (Fig. 2c). In comparison, the T-GNSs provided a pseudo-homogeneous intercalation environment for potassiation because the average *d*-spacing of the T-GNSs was smaller than that of KC_8. Moreover, the potassiation

potential did not change significantly, even when the *d*-spacing was increased by up to 50%. Hence, T-GNSs can show a two-phase-like plateau potential via solid-solution reactions.

To demonstrate the feasibility of T-GNSs in a full-cell system, we tested T-GNS-based full-cells. A graphitic nanocarbon (GNC), which can store PF_6 anions at high voltages (>4.5 V vs. K/K^+) via an anion intercalation mechanism, was used as the cathode material [55]. The material properties of the GNC are shown in Fig. S15. The GNC had a macroporous network structure composed of graphitic carbon nanofibers with an I_D/I_G ratio of 0.35 and d-spacing of ~ 0.34 nm. In the galvanostatic charge/discharge profiles in the voltage range 3.5–5.3 V vs. K/K^+, the GNC cathode demonstrated a reversible capacity of ~ 64 mA h g^{-1} with an average voltage of 4.64 V (Fig. S16a). When the GNC cathode was assembled with the T-GNS anode, the T-GNS//GNC full-cell profiles also demonstrated high-voltage performances (>4.5 V) with reversible capacities of ~ 46, ~40, ~35, and ~ 26 mA h g^{-1} at 0.1, 0.2, 0.4, and 1.0 A g^{-1}, respectively (Fig. S16b). The energy densities of the T-GNS//GNC full cells were ~ 205, ~180, ~160, and ~ 115 Wh kg^{-1} at power densities of ~ 450, ~900, ~1790, and ~ 4370 W kg^{-1}, respectively. The relatively high energy and power densities of the T-GNS//GNC full cells can be seen in the Ragone plots, which include the energy-power relationships of several potassium-ion storage devices (Fig. S16c) [56–62]. In addition, the T-GNS//GNC full cells revealed stable cycling performances over 100 cycles with similar capacity retentions (Fig. S16d). Hence, these full-cell data support the practicality of the T-GNSs as an anode for PIBs.

3. Conclusion

In summary, the effects of carbon microstructures on the potassium-ion storage behavior were investigated using two different nanocarbon materials, T-GNSs and GNPs, through a comparative study of lithium-ion and potassium-ion half-cells. The different local carbon microstructures led to vastly different lithium-ion storage behaviors between the T-GNSs and GNPs, while similar plateau-like capacities were observed at low voltages (~0.5 V) for potassium-ion storage. Interestingly, the defective T-GNSs had a higher plateau capacity (~200 mA h g^{-1}) than that of the GNPs (~120 mA h g^{-1}) with a large sloping capacity (~220 mA h g^{-1}). In addition, the T-GNSs showed higher rate capabilities, better reversibility, and more stable cycling performance. Ex situ Raman spectra characterized at different SoCs clearly demonstrated that the T-GNSs stored potassium ions via a solid-solution intercalation reaction with no phase transformation, which was very different from the two-phase reaction of the GNPs involving the formation of a new potassiation domain. Despite the similar plateau voltage profiles for the different charge storage mechanisms, the theoretical calculation data indicated that defective sites on the stacked graphene basal planes can diversify the potassiation redox potentials, where the electronic structure of the hexagonal carbon rings was highly affected by neighboring defective sites. The more metallic basal planes enhanced the electron affinity of the defective graphene surface, which enabled potassium to be adsorbed into a nearly stable monovalent state. This study reveals that defective graphitic materials are more suitable anode materials for PIBs.

Declaration of Competing Interest

The authors declare that they have no known competing financial interests or personal relationships that could have appeared to influence the work reported in this paper.

Acknowledgments

This research was supported by the Basic Science Research Program through the National Research Foundation of Korea (NRF) funded by the Ministry of Education (NRF-2019R1A2C1084836, and NRF-2021R1A4A2001403). This work was supported by the KU-KIST School Program.

Appendix A. Supplementary data

Supplementary data to this article can be found online at https://doi.org/10.1016/j.jechem.2021.11.027.

References

[1] J. Pramudita, D. Sehrawat, D. Goonetilleke, N. Sharma, Adv. Energy Mater. 7 (2017) 1602911.
[2] H. Kim, J.C. Kim, M. Bianchini, D.-H. Seo, J. Rodriguez-Garcia, G. Ceder, Adv. Energy Mater. 8 (2018) 1702384.
[3] T. Li, Q. Zhang, J. Energy Chem. 27 (2018) 373–374.
[4] X. Ge, S. Liu, M. Qiao, Y. Du, Y. Li, J. Bao, X. Zhou, Angew. Chem. Int. Ed. 58 (2019) 14578–14583.
[5] Y. Xu, Y. Du, Z. Yi, Z. Zhang, C. Lai, J. Liao, X. Zhou, J. Energy Chem. 58 (2021) 593–601.
[6] R.A. Adams, A. Varma, V.G. Pol, Adv. Energy Mater. 9 (2019) 1900550.
[7] K. Kubota, M. Dahbi, T. Hosaka, S. Kumakura, S. Komaba, Chem. Rec. 18 (2018) 459–479.
[8] H. He, D. Huang, Y. Tang, Q. Wang, X. Ji, H. Wang, Z. Guo, Nano Energy 57 (2019) 728–736.
[9] D.E. Nixon, G.S. Parry, J. Phys. D: Appl. Phys. 1 (1968) 291.
[10] W. Rüdorff, E. Schulze, Z. Anorg, Allg. Chem. 277 (1954) 156–171.
[11] W. Luo, J. Wan, B. Ozdemir, W. Bao, Y. Chen, J. Dai, H. Lin, Y. Xu, F. Gu, V. Barone, L. Hu, Nano Lett. 15 (2015) 7671–7677.
[12] J. Zhao, X. Zou, Y. Zhu, Y. Xu, C. Wang, Adv. Funct. Mater. 26 (2016) 8103–8110.
[13] J. He, T. Lu, K. Wang, X. Wang, X. Li, X. Shen, J. Gao, W. Si, Z. Yang, C. Huang, Adv. Funct. Mater. 31 (2021) 2005933.
[14] H.-J. Liang, B.-H. Hou, W.-H. Li, Q.-L. Ning, X. Yang, Z.-Y. Gu, X.-J. Nie, G. Wang, X.-L. Wu, Energy Environ. Sci. 12 (2019) 3575–3584.
[15] W. Wang, J. Zhou, Z. Wang, L. Zhao, P. Li, Y. Yang, C. Yang, H. Huang, S. Guo, Adv. Energy Mater. 8 (2018) 1701648.
[16] J. Yang, Z. Ju, Y. Jiang, Z. Xing, B. Xi, J. Feng, S. Xiong, Adv. Mater. 30 (2018) 1700104.
[17] M. Chen, W. Wang, X. Liang, S. Gong, J. Liu, Q. Wang, S. Guo, H. Yang, Adv. Energy Mater. 8 (2018) 1800171.
[18] J. Chen, B. Yang, H. Hou, H. Li, L. Liu, L. Zhang, X. Yan, Adv. Energy Mater. 9 (2019) 1803894.
[19] X. Hu, Y. Liu, J. Chen, L. Yi, H. Zhan, Z. Wen, Adv. Energy Mater. 9 (2019) 1901533.
[20] L. Liu, Y. Chen, Y. Xie, P. Tao, Q. Li, C. Yan, Adv. Funct. Mater. 28 (2018) 1801989.
[21] W. Zhang, Z. Cao, W. Wang, E. Alhajji, A.-H. Emwas, P.M.F.J. Costa, L. Cavallo, H. N. Alshareef, Angew. Chem. Int. Ed. 59 (2020) 4448–4455.
[22] J. Li, Y. Li, X. Ma, K. Zhang, J. Hu, C. Yang, M. Liu, Chem. Eng. J. 384 (2020) 123328.
[23] W. Yang, J. Zhou, S. Wang, W. Zhang, Z. Wang, F. Lv, K. Wang, Q. Sun, S. Guo, Energy Environ. Sci. 12 (2019) 1605–1612.
[24] G. Zhang, T. Guan, J. Qiao, J. Wang, K. Li, Energy Storage Mater. 26 (2020) 119–128.
[25] B.-Q. Li, C.-X. Zhao, J.-N. Liu, Q. Zhang, Adv. Mater. 31 (2019) 1808173.
[26] C.-X. Zhao, B.-Q. Li, Q. Zhang, J. Energy Chem. 34 (2019) 10–11.
[27] Z. Yi, J. Xu, Z. Xu, M. Zhang, Y. He, J. Bao, X. Zhou, J. Energy Chem. 60 (2021) 241–248.
[28] W. Han, G. Liu, W. Seo, H. Lee, H. Chu, W. Yang, Carbon 184 (2021) 534–543.
[29] X. Zhang, D. Chen, Y. Zhou, D. Yang, W. Liu, Y. Feng, X. Rui, Y. Yu, Chin. Chem. Lett. 32 (2021) 1161–1164.
[30] L. Xu, X. Chen, W. Guo, L. Zeng, T. Yang, P. Xiong, Q. Chen, J. Zhang, M. Wei, Q. Qian, Nanoscale 13 (2021) 5033–5044.
[31] B. Kang, X. Chen, L. Zeng, F. Luo, X. Li, L. Xu, M.-Q. Yang, Q. Chen, M. Wei, Q. Qian, J. Colloid Interface Sci. 574 (2020) 217–228.
[32] G. Kresse, J. Hafner, Phys. Rev. B 48 (1993) 13115.
[33] G. Kresse, J. Furthmüller, Phys. Rev. B 54 (1996) 11169.
[34] G. Kresse, D. Joubert, Phys. Rev. B 59 (1999) 1758.
[35] M. Dion, H. Rydberg, E. Schröder, D.C. Langreth, B.I. Lundqvist, Phys. Rev. Lett. 92 (2004) 246401.
[36] W. Tang, E. Sanville, G. Henkelman, J. Phys.-Condens. Matter 21 (2009) 084204.
[37] S.Y. Cho, Y.S. Yun, S. Lee, D. Jang, K.-Y. Park, J.K. Kim, B.H. Kim, K. Kang, D.L. Kaplan, H.-J. Jin, Nat. Commun. 6 (2015) 7145.
[38] Y.S. Yun, S. Lee, N.R. Kim, M. Kang, C. Leal, K.-Y. Park, K. Kang, H.-J. Jin, J. Power Sources 313 (2016) 142–151.
[39] X. Zheng, W. Chen, G. Wang, Y. Yu, S. Qin, J. Fang, F. Wang, X.-A. Zhang, AIP Adv. 5 (2015) 057133.

[40] L.G. Cançadoa, K. Takai, T. Enoki, Appl. Phys. Lett. 88 (2006) 163106.
[41] M. Endo, Y. Nishimura, T. Takahashi, K. Takeuchi, M.S. Dresselhaus, J. Phys. Chem Solids 57 (1996) 725–728.
[42] L. Zhang, W. Zhao, F. Jiang, M. Tian, Y. Yang, P. Ge, W. Sun, X. Ji, Sustain. Energ. Fuels 4 (2020) 3552–3565.
[43] Y.-F. Du, G.-H. Sun, Y. Li, J.-Y. Cheng, J.-P. Chen, G. Song, Q.-Q. Kong, L.-J. Xie, C.-M. Chen, Carbon 178 (2021) 243–255.
[44] N.R. Kim, S.M. Lee, M.W. Kim, H.J. Yoon, W.G. Hong, H.J. Kim, H.J. Choi, H.-J. Jin, Y.S. Yun, Adv. Energy Mater. 7 (2017) 1700629.
[45] M. Kühne, F. Börrnert, S. Fecher, M. Ghorbani-Asl, J. Biskupek, D. Samuelis, A.V. Krasheninnikov, U. Kaiser, J.H. Smet, Nature 564 (2018) 234–239.
[46] Y. Guo, Y. Wei, H. Li, T. Zhai, Small 13 (2017) 1701649.
[47] S.Y. Cho, M. Kang, J. Choi, M.E. Lee, H.J. Yoon, H.J. Kim, C. Leal, S. Lee, H.-J. Jin, Y. S. Yun, Small 14 (2018) 1703043.
[48] J. Xie, X. Li, H. Lai, Z. Zhao, J. Li, W. Zhang, W. Xie, Y. Liu, W. Mai, Angew. Chem. 131 (2019) 14882–14889.
[49] J. Liu, T. Yin, B. Tian, B. Zhang, C. Qian, Z. Wang, L. Zhang, P. Liang, Z. Chen, J. Yan, X. Fan, J. Lin, X. Chen, Y. Huang, K.P. Loh, Z.X. Shen, Adv. Energy Mater. 9 (2019) 1900579.
[50] V.A. Kislenko, S.V. Pavlov, S.A. Kislenko, Electrochim. Acta 341 (2020) 136011.
[51] J. Lahiri, Y. Lin, P. Bozkurt, I.I. Oleynik, M. Batzill, Nat. Nanotechnol. 5 (2010) 326–329.
[52] P. Kot, J. Parnell, S. Habibian, C. Straßer, P.M. Ostrovsky, C.R. Ast, Phys. Rev. B 101 (2020) 235116.
[53] D. Li, L. Dai, X. Ren, F. Ji, Q. Sun, Y. Zhang, L. Ci, Energy Environ. Sci. 14 (2021) 424–436.
[54] D. Li, X. Ren, Q. Ai, Q. Sun, L. Zhu, Y. Liu, Z. Liang, R. Peng, P. Si, J. Lou, J. Feng, L. Ci, Adv. Energy Mater. 8 (2018) 1802386.
[55] H.J. Yoon, N.R. Kim, H.-J. Jin, Y.S. Yun, Adv. Energy Mater. 8 (2018) 1701261.
[56] B. Ji, F. Zhang, N. Wu, Y. Tang, Adv. Energy Mater. 7 (2017) 1700920.
[57] D. Qiu, J. Guan, M. Li, C. Kang, J. Wei, Y. Li, Z. Xie, F. Wang, R. Yang, Adv. Funct. Mater. 29 (2019) 1903496.
[58] S. Dong, Z. Li, Z. Xing, X. Wu, X. Ji, X. Zhang, A.C.S. Appl, Mater. Interfaces 10 (2018) 15542–15547.
[59] J. Zhu, Y. Li, B. Yang, L. Liu, J. Li, X. Yan, D. He, Small 14 (2018) 1801836.
[60] L. Fan, Q. Liu, S. Chen, K. Lin, Z. Xu, B. Lu, Small 13 (2017) 1701011.
[61] M. Zhang, M. Shoaib, H. Fei, T. Wang, J. Zhong, L. Fan, L. Wang, H. Luo, S. Tan, Y. Wang, J. Zhu, J. Hu, B. Lu, Adv. Energy Mater. 9 (2019) 1901663.
[62] X. Ding, F. Zhang, B. Ji, Y. Liu, J. Li, C.-S. Lee, Y. Tang, A.C.S. Appl, Mater. Interfaces 10 (2018) 42294–42300.